Research Article

Wanzhuo Ma, Peng Yin, Mengmeng Li, Lu Sui, Tianshu Wang*, Zheqi Liu, Lei Du, Wenli Bao* and Yanqi Ge*

Graphdiyne-decorated microfiber based soliton and noise-like pulse generation

https://doi.org/10.1515/nanoph-2021-0299
Received June 14, 2021; accepted September 21, 2021; published online October 25, 2021

Abstract: Graphdiyne has an inborn band gap energy, where the minimal band gap is about from 0.46 to 1.22 eV, which shows great potential in ultrafast laser generation. In this work, we fabricate a graphdiyne-decorated microfiber and demonstrate its saturable absorption characteristics experimentally. This device is used as a saturable absorber to generate the conventional soliton and noise-like pulse in an erbium-doped mode-locked fiber laser. The conventional soliton with a spectral bandwidth of 2.45 nm can switch into noise-like pulse with 37.14 nm bandwidth by adjusting the pump power and the polarization controller. For the noise-like pulse, the mode-locked state has excellent stability with 2.17 nJ maximum pulse energy and 283 fs coherent peak duration. This work indicates that graphdiyne could be a remarkable nonlinear photonic device to explore the dynamics of various mode-locked pulses.

Keywords: graphdiyne; microfiber; mode-locked laser; noise-like pulse; soliton.

Wanzhuo Ma and Peng Yin contributed equally to this paper.

***Corresponding authors: Tianshu Wang**, College of Opto-Electronic Engineering, Changchun University of Science and Technology, Changchun 130022, China, E-mail: wangts@cust.edu.cn; **Wenli Bao** and **Yanqi Ge**, Institute of Microscale Optoelectronics, Collaborative Innovation Centre for Optoelectronic Science & Technology, International Collaborative Laboratory of 2D Materials for Optoelectronics Science and Technology of Ministry of Education, Key Laboratory of Optoelectronic Devices and Systems of Ministry of Education and Guangdong Province, College of Physics and Optoelectronic Engineering, Shenzhen Key Laboratory of Micro-Nano Photonic Information Technology, Guangdong Laboratory of Artificial Intelligence and Digital Economy (SZ), Shenzhen University, Shenzhen 518060, China, E-mail: geyanqi@hotmail.com (Y. Ge). https://orcid.org/0000-0001-7465-5665 (T. Wang)
Wanzhuo Ma, Mengmeng Li, Lu Sui, Zheqi Liu and Lei Du, College of Opto-Electronic Engineering, Changchun University of Science and Technology, Changchun 130022, China, E-mail: mawz@cust.edu.cn (W. Ma), 616581536@qq.com (M. Li), suilu@mails.cust.edu.cn (L. Sui), 769962323@qq.com (Z. Liu), leidu@mails.cust.edu.cn (L. Du)
Peng Yin, Institute of Microscale Optoelectronics, Collaborative Innovation Centre for Optoelectronic Science & Technology, International Collaborative Laboratory of 2D Materials for Optoelectronics Science and Technology of Ministry of Education, Key Laboratory of Optoelectronic Devices and Systems of Ministry of Education and Guangdong Province, College of Physics and Optoelectronic Engineering, Shenzhen Key Laboratory of Micro-Nano Photonic Information Technology, Guangdong Laboratory of Artificial Intelligence and Digital Economy (SZ), Shenzhen University, Shenzhen 518060, China, E-mail: yinpeng@szu.edu.cn. https://orcid.org/0000-0001-6355-3516

1 Introduction

Ultrafast fiber lasers have recently received rising interest owing to their narrow pulse duration, simple structure and low cost. It has been widely used in industrial processing [1], medical treatment [2], biomaterials [3], nonlinear optics [4–6], and other fields [7, 8]. As a nonlinear element, saturable absorber (SA) plays an essential role of mode-locked pulse generation in fiber lasers. The artificial SAs are commonly based on the nonlinear birefringence in fibers, such as nonlinear polarization rotation (NPR), nonlinear amplification loop mirror (NALM), which show a highly polarization-dependent, so that the mode-locking state is greatly affected by environments and difficult to achieve self-start [9]. Moreover, the narrow tuning range and complex fabrication process of one-dimensional real SAs such as semiconductor saturable absorber mirrors (SESAMs) [10] and single-walled carbon nanotubes (SWCNTs) urge the search for alternative SAs. The research on two-dimensional (2D) materials represented by graphene has advanced significantly. Ultrashort pulse mode-locked fiber lasers based on 2D materials, including graphene, transition metal dichalcogenides (TMDs), topological insulator, borophene [11], black phosphorus (BP) [12], MXene and so on have also drawn much attention due to their excellent nonlinearity.

In the anomalous dispersion region, soliton can easily convert into multiple soliton due to the peak power

clamping effect by increasing pump power in both artificial and real SAs based mode-locked fiber lasers [13, 14]. The interaction between multiple soliton pulses can induce the appearance of noise-like pulses (NLPs). Compared with the conventional soliton, the NLP has higher pulse energy [15], and its optical bandwidth can reach hundreds of nanometers [16]. The autocorrelation trace of a narrow peak on a broad pedestal shows that NLP has low coherence [17]. Therefore, NLP has advantages in grating sensing [18] and supercontinuum generation [19]. Many studies have explored the related applications of 2D materials as nonlinear materials. In 2014, Chen et al. use a novel SA topological insulator (TI) to study the formation of multi-soliton modes in erbium-doped fiber lasers, with a bandwidth of 9.3 nm of NLP [20]. In 2018, Wang et al. propose NLP with single pulse energy of 8.8 nJ at 1550 nm using the WS2-deposited microfiber structure [21]. In 2020, Wang et al. integrate Ti3C2 MXene into Tm:Ho codoped fiber laser and switch from vector soliton to NLP with a bandwidth of 3.3 nm by adjusting polarization controller (PC) [22]. Xu et al. report that the tellurene-based cone structure has good saturable absorption characteristics, and the pulse energy of NLP is 1.91 nJ [23]. In 2021, Tang et al. demonstrate the dynamic generation of NLPs and soliton rains in a graphene mode-locked fiber laser [24].

Currently, GDY is investigated more and more intensively due to its unique chemical structure and electronic properties [25, 26]. As a monoatomic layer allotrope of carbon materials, GDY has widely used in the fields of photoelectrochemical water splitting [27, 28], electrochemical catalysis [29], photodetectors [30], solar cells [31] and biomolecule sensing [32]. With the maturity of GDY synthesis technology and the gradual embodiment of its topological properties [33], the advantages of GDY as nonlinear material in the field of photonics are gradually reflected. First, it has a tunable direct bandgap in the range of 0.46–1.22 eV by changing the hydrogen coverage [34], which expands the application field of GDY. Also, the rich acetylene bonds and sub nanopores of GDY enable it to adjust the optical energy gap in a wide wavelength range and improve the compatibility of GDY [35]. Moreover, GDY has good stability and a high optical damage threshold. As the most stable carbon allotrope containing the diacetylene bond [36], GDY is significant to the development of long-term photonic devices. In 2019, Shi et al. propose the GDY-based hybrid mode-locking. The addition of the GDY structure reduces the pulse width by more than 50 fs, proving that GDY is expected to be used in ultrafast laser [37]. In 2020, Guo et al. use self phase modulation to demonstrate that GDY has broadband Kerr nonlinearity and a high nonlinear refractive index (about 10^{-15} cm^2) [38]. The mode-locked pulses are obtained at 1 and 1.5 μm by using GDY as an SA. They also report the chaos pulse in the 1.5 μm and the high-power pulse in the 2 μm [39]. Zu et al. propose an 1.9 μm all-solid-state Q-switched laser with GDY as an SA [40]. Zhang et al. realize a 2.1 um band Q-switched Ho^{3+} doped laser, which suggests that GDY is a promising candidate as an optical modulator [41]. The excellent Kerr nonlinearity of GDY illustrates that it possesses a promising application in nonlinear photonic devices [42]. All the above researches use the penetrating method to apply GDY in lasers, which has low thermal stability and is easy to damage the material. At present, the nonlinear research of GDY is still in the early stage. Especially in fiber lasers, few researches have been presented on the mode-locked pulse generation. Therefore it is essential to explore the nonlinear dynamics characteristics of GDY and its application potential in complex mock-locked pulses generation in fiber lasers.

In this work, we demonstrate that the GDY-coated microfiber composite structure can be used as a saturable absorption device to achieve the conversion between soliton pulse and NLP in the erbium-doped fiber laser cavity. Here, GDY is applied to fiber laser by the evanescent field method. The soliton pulse has a pulse duration of 2.21 ps. By increasing the pump power and controlling the PC appropriately, we obtain the NLP with 37.14 nm 3 dB spectrum bandwidth. The corresponding autocorrelation trace presents 90 ps pedestal and 283 fs coherent peak. The maximum pulse energy reaches 2.17 nJ at 950 mW of pump power. To our knowledge, this is the first time that NLP is generated in the anomalous dispersion region of GDY erbium-doped fiber laser.

2 Characteristics of GDY

In order to test the light response of graphdiyne nanosheets in neutral or acidic environments, a new synthesis method is used to obtain higher quality samples. Figure 1a demonstrates the transmission electron microscopy (TEM) image of the as-fabricated GDY while the individual flake is shown in Figure 1b. The overall morphology of graphdiyne prepared by ultrasonic manipulation can be clearly seen in the figure, which is more obvious than other two-dimensional materials previously studied [43, 44]. For the graphdiyne prepared by different methods and with different layers, the position and strength of the characteristic peaks are also very different. Especially noteworthy is the 2D peak of graphdiyne, the 2D peak shape of different layers of graphdiyne is very different. The obtained graphdiyne has very high carrier mobility, excellent

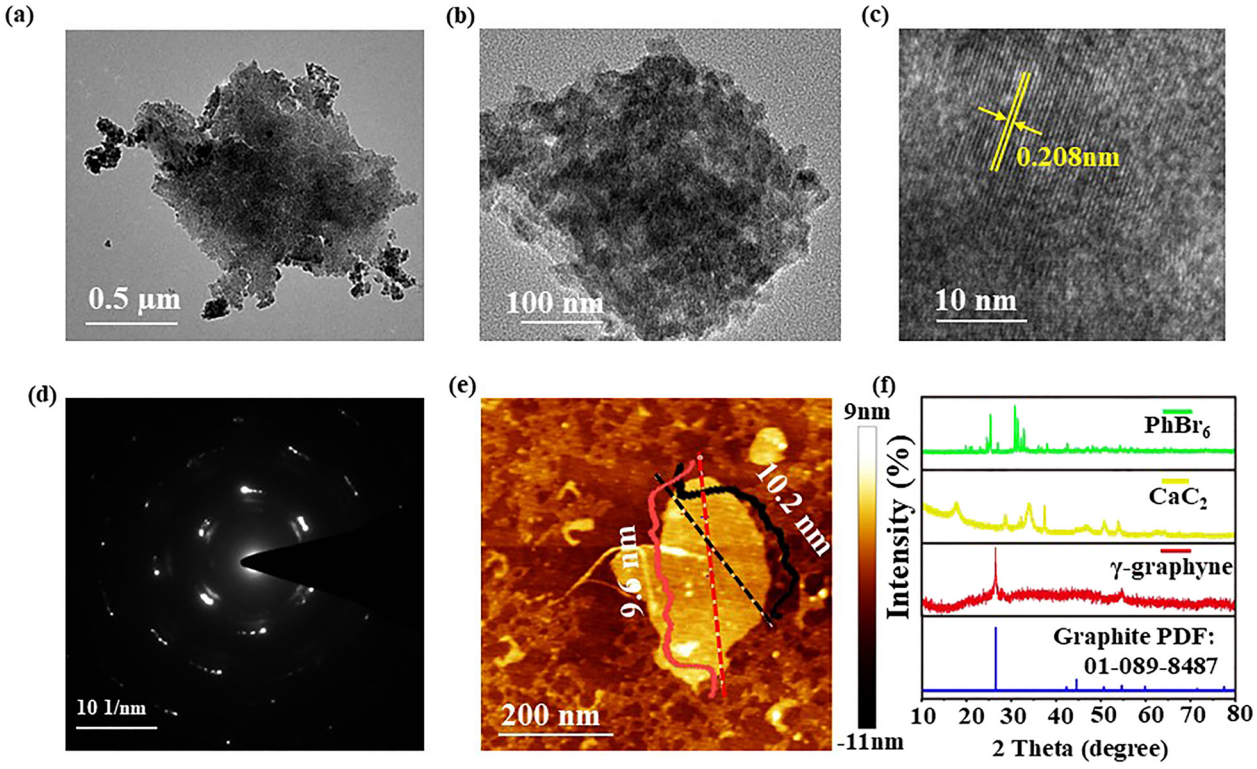

Figure 1: (a) TEM image in large scale, (b) TEM image of individual GDY flake, (c) HRTEM characterization of exfoliated graphdiyne, (d) SEAD pattern, (e) AFM cross section of graphdiyne nanosheets and (f) XRD spectra of graphdiyne nanosheets.

thermal conductivity and mechanical tensile strength, high transmittance to visible light, and very high specific surface area and other excellent properties, and has very high potential application value in many fields. Figure 1c shows a high-resolution transmission electron microscope (HRTEM) image of the sample and the corresponding selected electron diffraction pattern. It can be seen that the prepared graphdiyne has high purity, few defects and good crystallinity. The selected area electron diffraction (SAED) spectra of graphdiyne in different stacking modes were calculated as shown in Figure 1d [45]. The morphological characteristics and crystallographic properties of crystalline graphdiyne are analyzed by observing the micro-region correspondence between the selected morphology and the electron diffraction structure. The selected aperture blocks the electron beam outside the aperture so that the electron diffraction pattern observed on the fluorescent screen is due only to the contribution of crystals within the selected area. Different diffraction points are tested to observe the lattice distance. atomic force microscopy (AFM) characterization of graphdiyne nanosheets prepared on Si/SiO_2 substrates is shown in Figure 1e. The physical properties including morphology of the slices of the samples are detected, and the thickness of the graphdiyne nanosheets was 9.6 and 10.2 nm respectively, both of which are no more than 10.5 nm. The X-ray diffraction (XRD) patterns of four different samples are compared and analyzed. The test voltage is 40 kV and the external current is 40 mA. The experimental equipment is Cu-Kα Panalytical X ′PERT X-ray diffractive instrument installed in Holland. After experiments, the XRD pattern of PhBr6, CaC_2, graphdiyne, and graphite PDF card (JCPDS NO. 01-089-8487) are shown in Figure 1f. It can be seen that there is no characteristic diffraction peak in the XRD patterns of $PhBr_6$ and CaC_2, so PhBr6 and CaC_2 that are not involved in the reaction are completely eliminated in the purification process. It can be seen from the figure that graphdiyne has a very sharp and strong diffraction peak near 2θ of about 26°, that is, the diffraction peak on the (002) plane of graphdiyne. The diffraction peak proves that the spatial arrangement of the wafer layers is very regular at this time. Similarly, graphdiyne exhibits a diffraction peak near 2θ about 54°, namely the diffraction peak on the (004) plane of graphdiyne. However, the diffraction peak here becomes wider and the intensity decreases, which is caused by the decrease of the integrity of the crystal structure and the increase of disorder [43]. The phase composition of the sample can be qualitatively analyzed by comparing the XRD spectrum of the sample to be measured with that of the standard

substance. By analyzing and calculating the diffraction intensity data of the sample, the quantitative analysis of the phase composition of the sample can be completed. Some weak diffraction peaks are found in the XRD patterns of the samples, which have proved that these weak diffraction peaks are caused by graphite.

In addition, the open-aperture Z-scan measurements are carried out to acquire the nonlinear optical response of the GDY. The test results are fitted at 1550 and 1800 nm, respectively, as shown in Figure 2a and b. The normalized transmittance for GDY can be expressed as 8 [46]:

$$T(z) = 1 - \beta I_0 L_{\text{eff}} \Big/ \left(2^{\frac{3}{2}}\left(1 + z^2/z_0^2\right)\right) \tag{1}$$

where I_0 is the maximal intensity at Z = 0 mm; Z_0 is the Rayleigh range; $L_{\text{eff}} = [1 - \exp(-a_0 L)]/a_0$ is the effective thickness and α_0 is the linear absorption part which is independent of the optical intensity. The corresponding parameters are shown in Table 1. The value of β, about $-(1.53 \pm 0.03)$ cm GW^{-1}, can be calculated by combining the test results with the equation. The nonlinear transmission versus the incident intensity is also drawn in Figure 2c and d by extracting and converting the results of the OA Z-scan. The parameters of the GDY SA can be fitted with the one-photon absorption [47],

$$T(z) = 1 - A_s/(1 + I/I_s) - A_{\text{ns}} \tag{2}$$

where A_s and A_{ns} can be the modulation depth and nonsaturable loss, respectively; I_s is the saturation intensity. In addition, the closed aperture (CA) Z-scan approach is introduced to calculate the n_2 of the GDY SA. Figure 2e and f represent the normalized transmittance of the CA Z-scan data in condition of various wavelengths with the equation [48]:

$$T(z) = 1 - 4\Delta\Phi_0 x/[(x^2 + 1)(x^2 + 9)] \tag{3}$$

where $\Delta\Phi_0 = 2\pi n_2 I_0 L_{\text{eff}}/\lambda$ can be the phase conversion; $x = z/z_0$, ω_0 and λ is the beam waist and wavelength.

Furthermore, incident light with wavelengths of 800 and 850 nm is introduced to evaluate the polarization-dependent nonlinear optical absorption of the GYD saturable absorber with the polarization angle from 0° to 180° in a 45° step. The normalized transmittance increases first and tends to be stable at all polarization angles in condition of the sufficient incident power as shown in Figure 3, which indicates an SA response in the GDY flake for both excitations at 800 and 850 nm. However, the SA response at 800 nm possesses a much stronger dependence on the

Table 1: NLO performance of the GDY film at different wavelength.

λ	α_0 (cm^{-1})	β (cm GW^{-1})	I_s (GW cm^{-2})	n_2 (cm^2 W^{-1})
1550 nm	1.58×10^2	−1.53	4.29	0.35×10^{-5}
1800 nm	1.51×10^2	−1.44	2.36	0.54×10^{-5}

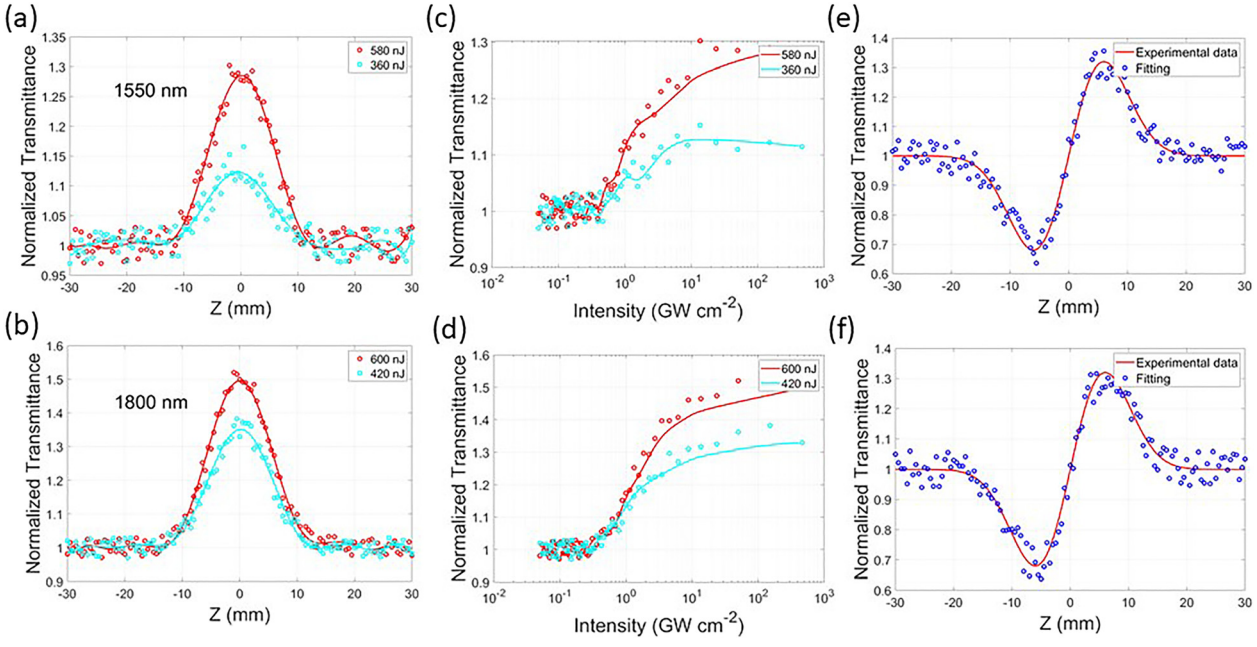

Figure 2: Characterization of the NLO properties of the GDY film. (a) and (b) The OA Z-scan tests of the GDY film at 1550 and 1800 nm, respectively. (c) and (d) Normalized transmittance versus the intensities at 1550 and 1800 nm, respectively. (e) and (f) The CA Z-scan tests of the GDY film at 1550 and 1800 nm, respectively.

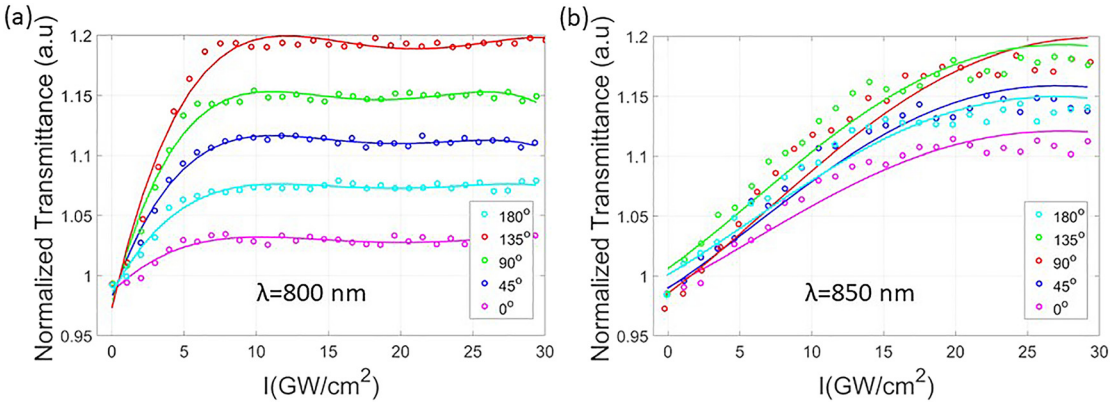

Figure 3: Experimental data and fitting curves of the polarization-dependent SA response with incident wavelength of (a) 800 and (b) 850 nm.

polarization of the incident light, which indicates a smaller absolute modulation depth appeared at 800 nm. This is because the photon energy at 850 nm is closer to the bandgap than that at 800 nm, which induces more absorption.

3 Fabrication and nonlinear absorption characteristics of GDY-decorated microfiber

We fabricate the microfiber tapers decorated with GDY. First, a fiber with the diameter of subwavelength taper is prepared from a standard single-mode silica fiber and place it on a glass slide. Then, the sample solution is deposited over the waist part of the silica fiber by the photodeposition method. Afterward, the sample is dried under room temperature. Figure 4a shows the structure of the hybrid waveguide under a microscope. The working principle of the GDY-decorated microfiber is the interaction between GDY and transmitted light in the evanescent field. The core of microfiber belongs to the subwavelength range, which can make light propagate along the fiber surface through an evanescent field [49]. The light is attracted to the GDY film layer through the evanescent field, which ensures that there are enough light fields for light–matter interaction. Using red light in the composite structure, one can see the light field around the cone region, as shown in Figure 4 (b). Figure 4 (c) is the structure under the microscope. This evanescent field action can enhance the nonlinearity of the cavity [21] and make the material have a high damage threshold. In our experiment, the silica microfiber is fabricated with 7 μm in diameter and 1 cm in length. This tapered fiber structure can enhance the effective action length of GDY remarkably. The depositional length is approximately 6 mm. To reduce the impact of the external environment, the GDY-decorated microfiber is fixed on a glass slide. It should be noted that the direct contact between the microfiber and glass slide will lead to additional confined loss because they have similar refractive index. We set the spacing between the microfiber and the glass slide to about 0.5 mm, which is an order of magnitude higher than the diameter of microfiber. In this case, the insertion loss of the fiber is monitored at 1.8 dB during the experiment.

The nonlinear absorption characteristic of the GDY-decorated microfiber is investigated using the dual-power

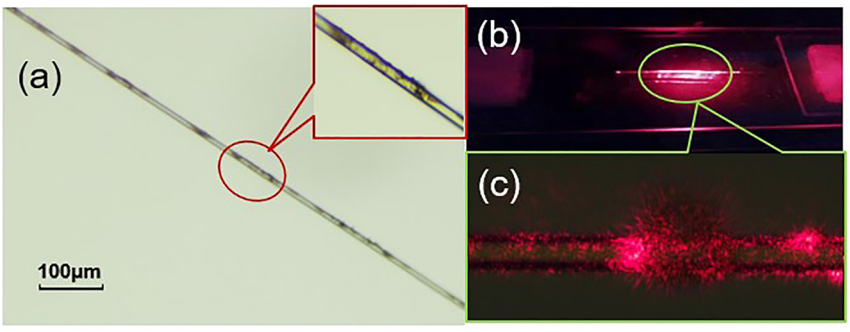

Figure 4: (a) Images of GDY-decorated microfiber under microscope. Illustration shows the closeup views of GDY. (b) The composite structure under red light. (c) The closeup views of (b) under microscope.

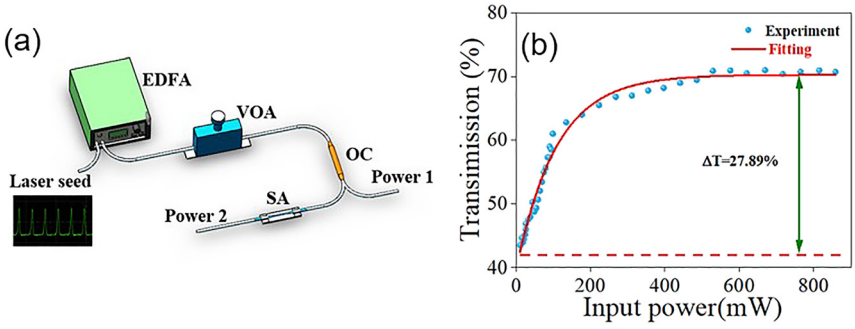

Figure 5: (a) Dual channel detector, (b) transmission curves of GDY saturable absorber.

detection method. Figure 5a shows the measurement device. A 1559.6 nm homemade ultrashort pulse light with a repetition frequency of 22.65 MHz and a pulse duration of 2.13 ps serves as the seed source. The laser seed respectively passes through an erbium-doped fiber amplifier (EDFA) and variable optical attenuator (VOA) to ensure that the material is bleached. Then, the light is divided into two channels through a 3 dB optical coupler (OC). The reference channel is directly output, and the test one is entering SA. We record the output power and calculate the modulation depth, as shown in Figure 5b. The modulation depth of SA is 27.89%, which is an ideal SA for mode-locking.

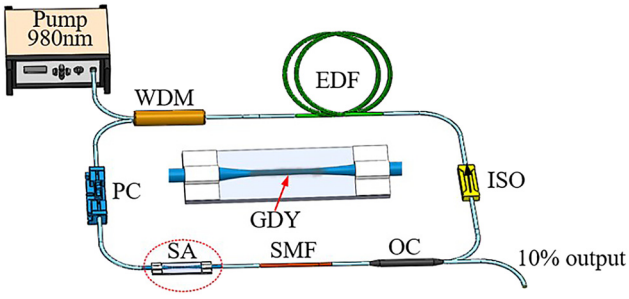

Figure 6: Experimental setup of GDY-based SA mode-locked EDF laser.

4 Experimental setup

The experiment setup of passively mode-locked laser cavity based on GDY-decorated microfiber is shown in Figure 6. A 980 nm laser diode with a maximum power of 1 W is used to pump a segment of 2 m erbium-doped fiber (EDF) through wavelength division multiplexer (WDM, 980/1550 nm). The unidirectional operation of the laser cavity is controlled by a polarization-insensitive isolator (ISO), and the experiment is backward pumping. The PC is used to optimize the performance of the mode-locked laser. The saturable absorption element is a GDY-decorated microfiber composite structure. A 15.5 m single-mode fiber (SMF) is added to increase the nonlinearity. A 90:10 coupler (OC) is used for mode-locked pulse output, extracting 10% of the power measurement to ensure a high enough power within the cavity. The group velocity dispersions (GVDs) of EDF and SMF are 31 ps^2 km^{-1}, −22.94 ps^2 km^{-1} at 1550 nm, respectively. The total cavity length and net dispersion are 22.1 m, −0.34 ps^2. Optical spectrum and temporal profiles are analyzed by an optical spectrum analyzer (OSA, Yokogawa AQ6375) and an oscilloscope (OSC, Agilent 86100C). The frequency domain is monitored by a frequency spectrum analyzer (FSA, Agilent N9030A). The duration of solitons and NLPs are measured by a commercial autocorrelator (Femtochrome FR-103XL).

5 Results and discussions

First, we insert a microfiber without depositing GDY into the laser cavity. By controlling the pump power and the polarization state, the absence of a mode-locking pulse indicates that the component does not contribute to the passively mode-locking in an erbium-doped fiber laser. After replacing the microfiber with the SA, we find that the cavity is still working in the form of continuous light under low power conditions. When the pump power is increased to 380 mW the mode-locking can be achieved due to the excellent saturable absorption of GDY-decorated microfiber. The high threshold of mode-locking is due to the evanescent field structure. The pump light interacts with GDY indirectly, with high saturation light intensity, which raises the mode-locking threshold relatively. In this case, the soliton formed in the fiber laser is due to the balance of dispersion and nonlinearity. Figure 7a shows optical spectra of conventional soliton in the anomalous dispersion region. During the period of soliton amplification, soliton propagation will cause instability characterized by

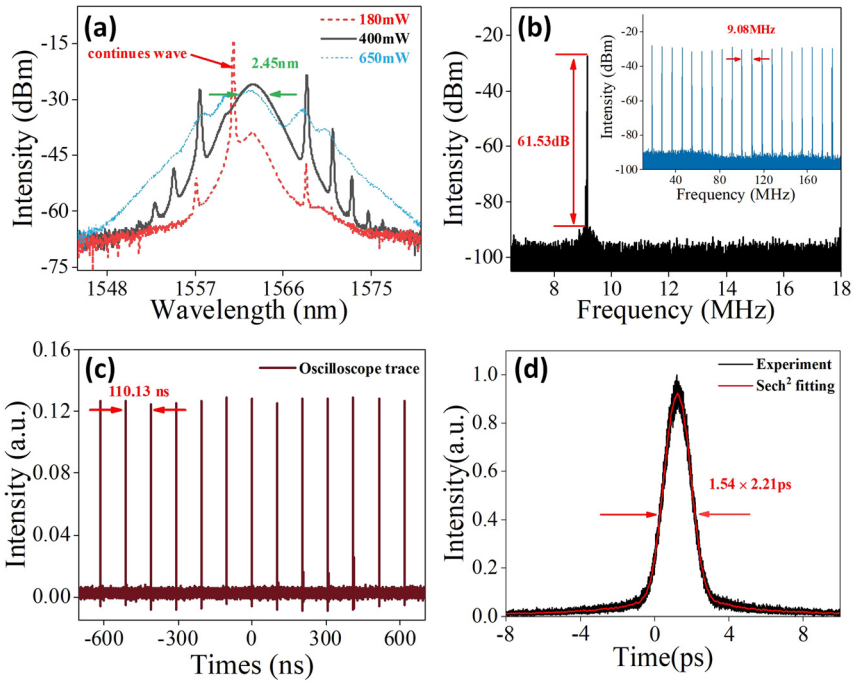

Figure 7: Mode-locking characteristics of soliton, (a) the optical spectra of soliton state, (b) the RF spectrum of soliton state, (c) mode-locked pulse trace of soliton state at 400 mW, (d) autocorrelation trace of soliton state at 400 mW.

discrete sideband structure [50], so the Kelly-sidebands are distributed on both sides of the spectrum symmetrically. The soliton mode-locking state remains stable even when the pump power is reduced to 180 mW, but some continuous light is doped, shown as the red dotted line in Figure 7a. Once the soliton pulse disappears, the power must be increased to the mode-locking threshold before the mode-locking can be realized again. This phenomenon has been proved to be pump power hysteresis [51]. Figure 7b shows the corresponding RF spectrum at 400 mW pump power. The optical signal-to-noise ratio (OSNR) is 61.53 dB, and the illustration is a 200 MHz broadband RF spectrum, which proves the excellent stability of the mode-locking. In the time domain, the pulse trace of soliton shows excellent stability between 180 and 650 mW pump power, as shown in Figure 7c. The separation between adjacent pulses is 110.13 ns which correspond to the fundamental repetition rate of 9.08 MHz. Figure 7d shows the measured autocorrelation trace with a pulse duration of 2.21 ps and a time-bandwidth product (TBP) of 0.66, indicating that the pulse is slightly chirped.

The high damage threshold of the GDY-decorated microfiber can ensure the laser working under a high pump power, which can help the soliton split into multiple pulses in the anomalous dispersion region [52]. At 650 mW pump power, the mode-locking pulse of soliton becomes unstable, with the Kelly side-bands is suppressed and weakened, as shown by the blue dotted line in Figure 7a. When pump power increases to 760 mw, the optical spectrum is extended and smoothed by adjusting the PC. Various soliton mode-locking states have been achieved in this work by controlling PC, such as soliton beam, chaotic multi-soliton, harmonic mode-locking, etc. In addition to generating various soliton states, the interaction of multiple pulses can also induce the generation of NLP [21]. When the pump power increases, the mode-locking states become unstable due to the saturation absorption effect, and soliton collapse occurs. Then, the NLP operates at the fundamental repetition rate [53]. Figure 8a is the spectrum at 950 mW. We obtain the NLP with a 3 dB bandwidth of 37.14 nm. The RF spectrum is shown in Figure 8b, with the OSNR of 54.6 dB. The NLP operates at a 9.08 MHz fundamental repetition rate, which corresponds to theoretical calculation. Noise-like pulse is a wave packet composed of a large number of ultrashort pulses, which is a phenomenon of random coexistence and bunching of multiple soliton pulses that cannot be separated in the time domain [21, 54, 55]. Experimental results show that a stable oscilloscope trace of NLP is obtained at 760 mw, as shown in Figure 8c. The mode-locked state can be maintained until the power decreases to 620 mw. Fixing pump power at 950 mW, Figure 8d shows that the autocorrelation trace has a broad pedestal of 90 ps approximately, which is a typical characteristic of NLP. The coherent peak duration is 283 fs, as shown in the illustration of Figure 8d.

This experiment achieves stable conventional soliton mode-locking at 180–650 mW and operates in a steady noise-like state at 620–950 mW. Figure 9 shows the average

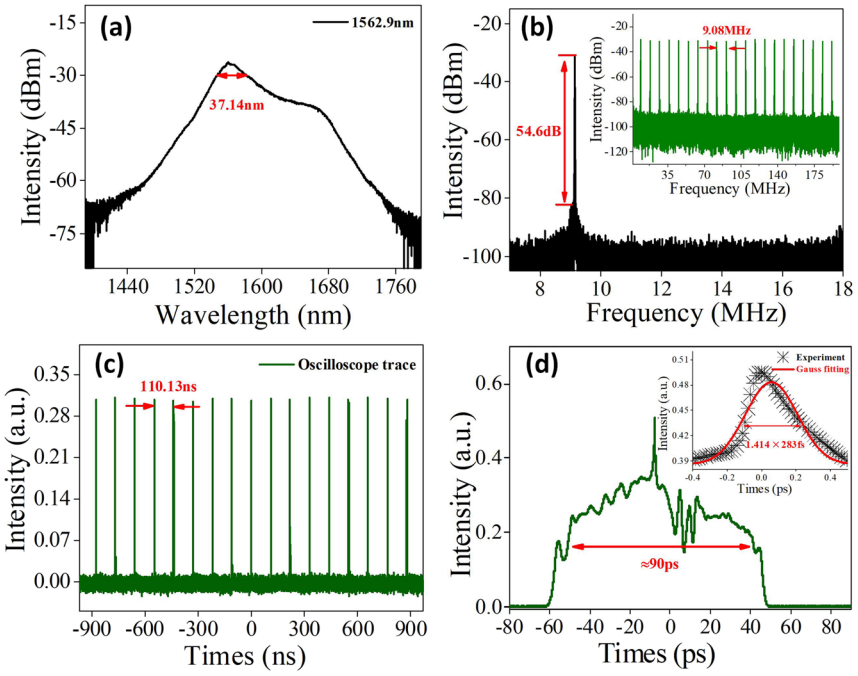

Figure 8: Mode-locking characteristics of NLP, (a) the optical spectrum of NLP state, (b) the RF spectrum of NLP state. (c) Mode-locked pulse trace of NLP state at 950 mW, (d) autocorrelation trace of NLP state at 950 mW.

output power and single pulse energy of soliton pulse and NLP against pump power. It is observed that the average output power and single pulse energy grow linearly with the increase of pump power. The maximum average output power of the soliton is 8.4 mW at 650 mW, corresponding to the single pulse energy of 0.93 nJ. For NLP, 950 mW pump power with an output power of 19.69 mW, while the single pulse energy is 2.17 nJ. Obviously, the NLP has higher output power and pulse energy than the conventional soliton, which is consistent with the characteristics of NLP, so it can be confirmed that this is a typical NLP mode-locking mechanism. The average output power of the NLP does not show saturation, indicating that the pulse energy will be improved with the increase of pump power. In the range of 620–650 mW, both the conventional soliton and the noise-like can operate stably, which are determined by the pump power hysteresis, the intracavity birefringence, and the saturation absorption effect.

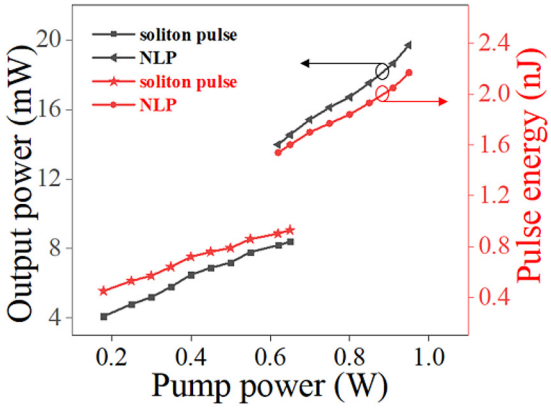

Figure 9: The average output power and single pulse energy of soliton pulse and NLP against pump power.

Figure 10a shows the spectral evolutions of NLP at different pump powers. With the increase of pump power, the intensity of the spectrum grows steadily and broadens slowly. In Figure 10b, the 3 dB bandwidth and pulse duration of NLP will vary with different pump powers. When the pump power increases from 620 to 950 mW, the spectral bandwidth broadens from 33.72 to 37.14 nm, and the bandwidth expanded by 3.42 nm. On the contrary, the coherent peak duration decreases from 314 fs to 283 fs.

To confirm the stability of NLP, we measured the optical spectrum, autocorrelation trace and output power of the ultrashort pulse at 950 mW. Based on the above findings, the spectral bandwidth and pulse energy were calculated. The statistical results are shown in Figure 11, where a set of data is recorded every 5 min within an hour. Figure 11a shows that the range of central wave-length and the spectral bandwidth is 1562.9–1563.05 nm, 33.41–37.14 nm, respectively. The variation of the coherent peak duration of a narrow spike is 1.34 fs in Figure 11b, which can reflect femtosecond pulse oscillation with randomly varying width inside the envelope. The average output power and single pulse energy of the mode-locked pulse remain almost unchanged, as shown in Figure 11c. During the whole process, the mode-locking state is not interrupted. This experiment proves that the passively mode-locked system with GDY as SA can output NLP in a highly stable condition. The generation of NLP proves that the

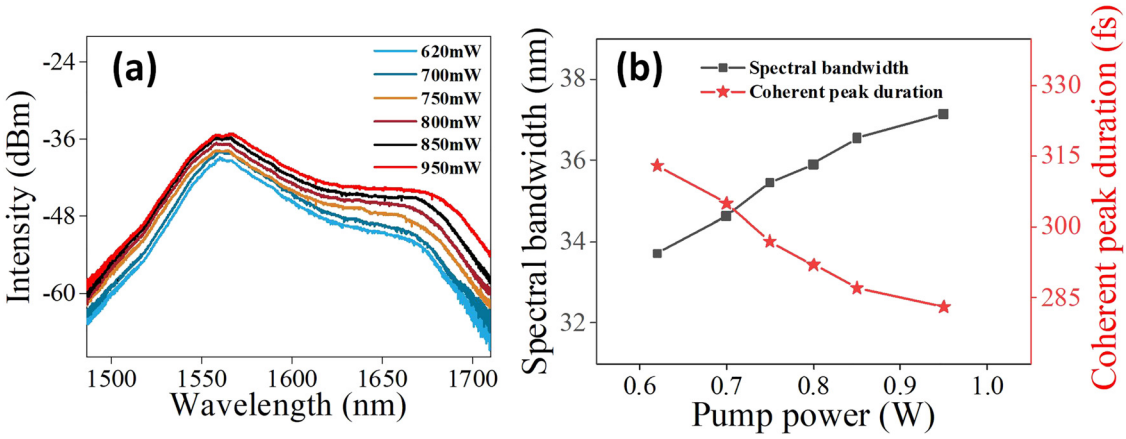

Figure 10: The characteristics of NPL at different pump powers, (a) spectra at different pump power, (b) curves of spectral bandwidth and pulse duration with different pump power.

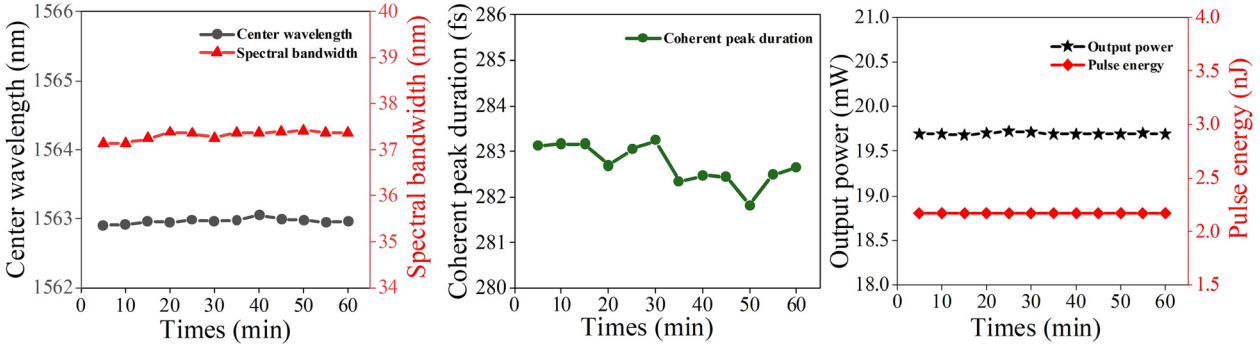

Figure 11: Stability of passively mode-locked NLP output of GDY saturable absorber, (a) center wavelength and spectral bandwidth against times, (b) coherent peak duration against times, (c) output power and pulse energy against times.

mode-locked laser has the ability to work at high pump power, indicating that it has great potential in the generation of other high-energy mode-locking states such as dissipative solitons, broadening pulses and self similar pulses in positive dispersion and dispersion management region.

6 Conclusions

In conclusion, the conventional soliton and NLP are successfully generated in the erbium-doped fiber laser by using the GDY-decorated microfiber composite structure as the saturation absorption device. The experimental results show that the spectral bandwidth of the conventional soliton is 2.45 nm, the pulse duration is 2.21 ps at 400 mW, and the maximum pulse energy is 0.93 nJ. With a high pump power, the spectral bandwidth of the NLP is 37.14 nm, the duration of coherent peak on the broad pedestal is 283 fs. The corresponding maximum pulse energy is 2.17 nJ. The two modes operate at the same repetition rate of 9.08 MHz. This work promotes the application of 2D materials in fiber lasers and confirms that GDY is expected to play a significant role in nonlinear dynamics.

Author contribution: All the authors have accepted responsibility for the entire content of this submitted manuscript and approved submission.

Research funding: This work was supported by the National Natural Science Foundation of China under Grant (61975021, 62005024, 61905022), the Natural Science Foundation of Jilin Province (YDZJ202101ZYTS139), and the Research Project of Jilin Provincial Education Department under Grant (JJKH20210816KJ).

Conflict of interest statement: The authors declare no conflicts of interest regarding this article.

References

[1] M. Hu, Y. Zheng, and Y. Yang, "Nanosecond double-pulse fiber laser with arbitrary sub-pulse combined based on a spectral beam combining system," *Opt. Laser. Technol.*, vol. 90, pp. 22–26, 2017.

[2] N. Mamalis, "Femtosecond laser: the future of cataract surgery," *J. Cataract Refract. Surg.*, vol. 37, pp. 1177–1178, 2011.

[3] R. F. de Menezes, C. M. Harvey, M. E. M. de Martínez Gerbi, et al., "Fs-laser ablation of teeth is temperature limited and provides information about the ablated components," *J. Biophot.*, vol. 10, pp. 1292–1304, 2017.

[4] M. Bagheri, C. Frez, and L. A. Sterczewski, "Passively mode-locked interband cascade optical frequency combs," *Sci. Rep.*, vol. 8, pp. 1–7, 2018.

[5] S. Tozburun, C. Blatter, and M. Siddiqui, "Phase-stable Doppler OCT at 19 MHz using a stretched-pulse mode-locked laser," *Biomed. Opt. Express*, vol. 9, pp. 952–961, 2018.

[6] S. V. Smirnov, S. M. Kobtsev, and S. V. Kukarin, "Efficiency of non-linear frequency conversion of double-scale pico-femtosecond pulses of passively mode-locked fiber laser," *Opt. Express*, vol. 22, pp. 1058–1064, 2014.

[7] P. Yin, X. Jiang, R. Huang, et al., "2d materials for nonlinear photonics and electro-optical applications," *Adv. Mater. Interfaces*, vol. 8, p. 2100367, 2021.

[8] Q. Tian, P. Yin, T. Zhang, et al., "Mxene Ti3c2tx saturable absorber for passively Q-switched mid-infrared laser operation of femtosecond-laser–inscribed Er:Y2o3 ceramic channel waveguide," *Nanophotonics*, vol. 9, pp. 2495–2503, 2020.

[9] K. Tamura, H. A. Haus, and E. P. Ippen, "Self-starting additive pulse mode-locked erbium fibre ring laser," *Electron. Lett.*, vol. 28, pp. 2226–2228, 1992.

[10] U. Keller, "Recent developments in compact ultrafast lasers," *Nature*, vol. 424, pp. 831–838, 2003.

[11] C. Ma, P. Yin, and K. Khan, "Broadband nonlinear photonics in few-layer borophene," *Small*, vol. 17, p. 2006891, 2021.

[12] Z. Qin, G. Xie, and C. Zhao, "Mid-infrared mode-locked pulse generation with multilayer black phosphorus as saturable absorber," *Opt. Lett.*, vol. 41, pp. 56–59, 2016.

[13] D. Y. Tang, L. M. Zhao, and B. Zhao, "Mechanism of multisoliton formation and soliton energy quantization in passively mode-locked fiber lasers," *Phys. Rev.*, vol. 72, 2005, Art no. 043816.

[14] C. Ma, P. Yin, K. Khan, et al., "Broadband nonlinear photonics in few-layer borophene," *Small*, vol. 17, p. 2006891, 2021.

[15] X. W. Zheng, Z. C. Luo, and H. Liu, "High-energy noiselike rectangular pulse in a passively mode-locked figure-eight fiber laser," *APEX*, vol. 7, 2014, Art no. 042701.

[16] L. M. Zhao, D. Y. Tang, and T. H. Cheng, "120 nm bandwidth noise-like pulse generation in an erbium-doped fiber laser," *Opt. Commun.*, vol. 281, pp. 157–161, 2008.

[17] Z. Wang, Z. Wang, and Y. Liu, "Q-switched-like soliton bunches and noise-like pulses generation in a partially mode-locked fiber laser," *Opt. Express*, vol. 24, pp. 14709–14716, 2016.

[18] V. Goloborodko, S. Keren, and A. Rosenthal, "Measuring temperature profiles in high-power optical fiber components," *Appl. Opt.*, vol. 42, pp. 2284–2288, 2003.

[19] A. Zaytsev, C. H. Lin, and Y. J. You, "Supercontinuum generation by noise-like pulses transmitted through normally dispersive standard single-mode fibers," *Opt. Express*, vol. 21, pp. 16056–16062, 2013.

[20] Y. Chen, M. Wu, and P. Tang, "The formation of various multi-soliton patterns and noise-like pulse in a fiber laser passively mode-locked by a topological insulator based saturable absorber," *Laser Phys. Lett.*, vol. 11, 2014, Art no. 055101.

[21] Z. Wang, Z. Wang, and Y. Liu, "Noise-like pulses generated from a passively mode-locked fiber laser with a WS_2 saturable absorber on microfiber," *Laser Phys. Lett.*, vol. 15, 2018, Art no. 085103.

[22] S. Wang, L. Li, and Y. Song, "Vector soliton and noise-like pulse generation using a Ti_3C_2 MXene material in a fiber laser," *Front. Inf. Technol. Electron. Eng.*, pp. 1–7, 2020.

[23] N. Xu, P. Ma, and S. Fu, "Tellurene-based saturable absorber to demonstrate large-energy dissipative soliton and noise-like pulse generations," *Nanophotonics*, vol. 9, pp. 2783–2795, 2020.

[24] P. Tang, M. Luo, and T. Zhao, "Generation of noise-like pulses and soliton rains in a graphene mode-locked erbium-doped fiber ring laser," *Front. Inf. Technol. Electron. Eng.*, vol. 22, pp. 303–311, 2021.

[25] C. Huang, Y. Zhao, and Y. Li, "Graphdiyne: the fundamentals and application of an emerging carbon material," *Adv. Mater.*, vol. 31, p. 1904885, 2019.

[26] G. Li, Y. Li, and H. Liu, "Architecture of graphdiyne nanoscale films," *Chem. Commun.*, vol. 46, pp. 3256–3258, 2010.

[27] J. Li, X. Gao, and X. Jiang, "Graphdiyne: a promising catalyst–support to stabilize cobalt nanoparticles for oxygen evolution," *ACS Catal.*, vol. 7, pp. 5209–5213, 2017.

[28] Y. Xue, Z. Zuo, and Y. Li, "Graphdiyne-supported $NiCo_2S_4$ nanowires: a highly active and stable 3D bifunctional electrode material," *Small*, vol. 13, p. 1700936, 2017.

[29] L. Xiuli, H. Yingying, and L. Tongbu, "Structure characterization and application of graphdiyne in photocatalytic and electrocatalytic reactions," *Acta Phys.-Chim. Sin.*, vol. 34, pp. 1014–1028, 2018.

[30] P. Yin, W. Bao, L. Gao, et al., "Performance analysis of photo-electrochemical photodetector based on liquid-phase exfoliation few-layered graphdiyne nanosheets," *Nanophotonics*, vol. 10, pp. 2833–2845, 2021.

[31] X. Wang, "Chemically synthetic graphdiynes: application in energy conversion fields and the beyond," *Sci. China Mater.*, vol. 58, pp. 347–348, 2015.

[32] N. Parvin, Q. Jin, and Y. Wei, "Few-layer graphdiyne nanosheets applied for multiplexed real-time DNA detection," *Adv. Mater.*, vol. 29, p. 1606755, 2017.

[33] X. L. Sheng, C. Chen, H. Liu, et al., "Two-dimensional second-order topological insulator in graphdiyne," *Phys. Rev. Lett.*, vol. 123, p. 256402, 2019.

[34] Y. Li, L. Xu, and H. Liu, "Graphdiyne and graphyne: from theoretical predictions to practical construction," *Chem. Soc. Rev.*, vol. 43, pp. 2572–2586, 2014.

[35] H. Yu, Y. Xue, and Y. Li, "Graphdiyne and its assembly architectures:synthesis, functionalization, and applications," *Adv. Mater.*, vol. 31, p. 1803101, 2019.

[36] C. Lu, Y. Yang, and J. Wang, "High-performance graphdiyne-based electrochemical actuators," *Nat. Commun.*, vol. 9, pp. 1–11, 2018.
[37] Z. Shi, X. Li, and Y. Zhang, "Graphdiyne for ultrashort pulse generation in an erbium-doped hybrid mode-locked fiber laser," *Front. Phys.*, vol. 7, p. 150, 2019.
[38] J. Guo, R. Shi, and R. Wang, "Graphdiyne-polymer nanocomposite as a broadband and robust saturable absorber for ultrafast photonics," *Laser Photon. Rev.*, vol. 14, p. 1900367, 2020.
[39] J. Guo, Z. Wang, R. Shi, et al., "Graphdiyne as a promising mid-infrared nonlinear optical material for ultrafast photonics," *Adv. Opt. Mater.*, vol. 8, p. 2000067, 2020.
[40] Y. Zu, J. Guo, and Q. Hao, "Graphdiyne as a saturable absorber for 2-μm all-solid-state Q-switched laser," *Sci. China Mater.*, pp. 1–8, 2020.
[41] C. Zhang, Q. Hao, and Y. Zu, "Graphdiyne saturable absorber for passively Q-switched Ho^{3+}-doped laser," *Nanomaterials*, vol. 10, p. 1848, 2020.
[42] L. Wu, Y. Dong, and J. Zhao, "Kerr nonlinearity in 2D graphdiyne for passive photonic diodes," *Adv. Mater.*, vol. 31, p. 1807981, 2019.
[43] Y. Li, Q. Liu, W. Li, H. Meng, Y. Lu, and C. Li, "Synthesis and supercapacitor application of alkynyl carbon materials derived from Cac2 and polyhalogenated hydrocarbons by interfacial mechanochemical reactions," *ACS Appl. Mater. Interfaces*, vol. 9, pp. 3895–3901, 2017.
[44] Y. Li, Q. Liu, W. Li, Y. Lu, H. Meng, and C. Li, "Efficient destruction of hexachlorobenzene by calcium carbide through mechanochemical reaction in a planetary ball mill," *Chemosphere*, vol. 166, pp. 275–280, 2017.
[45] R. Matsuoka, R. Sakamoto, K. Hoshiko, et al., "Crystalline graphdiyne nanosheets produced at a gas/liquid or liquid/liquid interface," *J. Am. Chem. Soc.*, vol. 139, pp. 3145–3152, 2017.
[46] Y. Ge, S. Chen, Y. Xu, et al., "Few-layer selenium-doped black phosphorus: synthesis, nonlinear optical properties and ultrafast photonics applications," *J. Mater. Chem. C*, vol. 5, pp. 6129–6135, 2017.
[47] Y. Ge, Z. Zhu, Y. Xu, et al., "Broadband nonlinear photoresponse of 2d Tis2 for ultrashort pulse generation and all-optical thresholding devices," *Adv. Opt. Mater.*, vol. 6, p. 1701166, 2018.
[48] M. Sheik-Bahae, A. A. Said, T.-H. Wei, D. J. Hagan, and E. W. Van Stryland, "Sensitive measurement of optical nonlinearities using a single beam," *IEEE J. Quant. Electron.*, vol. 26, pp. 760–769, 1990.
[49] B. C. Yao, Y. Wu, and A. Q. Zhang, "Graphene enhanced evanescent field in microfiber multimode interferometer for highly sensitive gas sensing," *Opt. Express*, vol. 22, pp. 28154–28162, 2014.
[50] S. M. J. Kelly, "Characteristic sideband instability of periodically amplified average soliton," *Electron. Lett.*, vol. 28, pp. 806–807, 1992.
[51] M. Nakazawa, E. Yoshida, and Y. Kimura, "Low threshold, 290 fs erbium-doped fiber laser with a nonlinear amplifying loop mirror pumped by InGaAsP laser diodes," *Appl. Phys. Lett.*, vol. 59, pp. 2073–2075, 1991.
[52] D. Y. Tang, L. M. Zhao, and B. Zhao, "Mechanism of multisoliton formation and soliton energy quantization in passively mode-locked fiber lasers," *Phys. Rev.*, vol. 72, 2005, Art no. 043816.
[53] L. M. Zhao, D. Y. Tang, and J. Wu, "Noise-like pulse in a gain-guided soliton fiber laser," *Opt. Express*, vol. 15, pp. 2145–2150, 2007.
[54] R. Zhou, X. Liu, and D. Yu, "Versatile multi-soliton patterns of noise-like pulses in a passively mode-locked fiber laser," *Opt. Express*, vol. 28, pp. 912–923, 2020.
[55] V. Voropaev, A. Donodin, and A. Voronets, "Generation of multi-solitons and noise-like pulses in a high-powered thulium-doped all-fiber ring oscillator," *Sci. Rep.*, vol. 9, pp. 1–11, 2019.